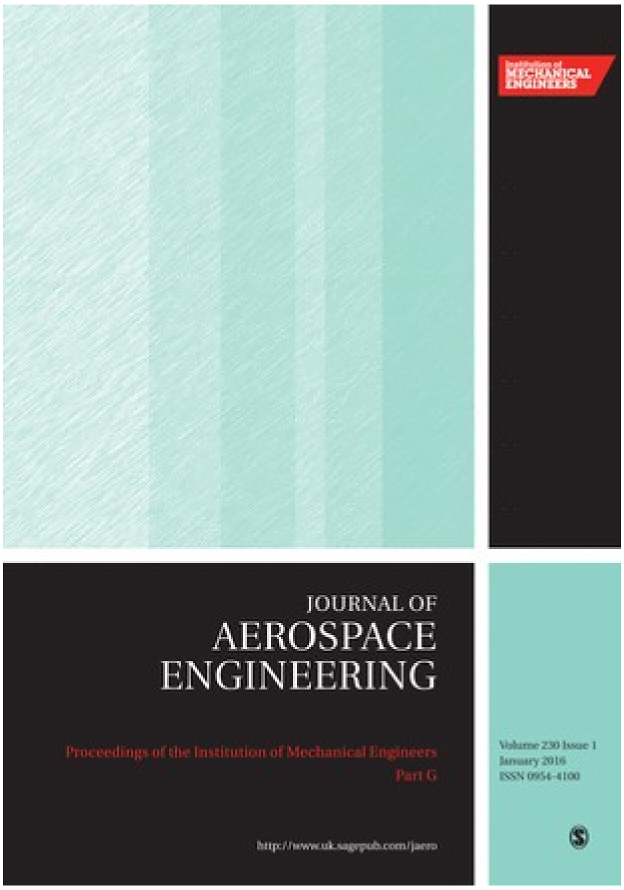

Institution of MECHANICAL ENGINEERS

JOURNAL OF
AEROSPACE ENGINEERING

Proceedings of the Institution of Mechanical Engineers
Part G

http://www.uk.sagepub.com/jaero

Volume 230 Issue 1
January 2016
ISSN 0954-4100

Volume 230 Number 1 January 2016

Institution of MECHANICAL ENGINEERS

Journal of AEROSPACE ENGINEERING

Contents

Original Articles

Original Article

Institution of MECHANICAL ENGINEERS

Journal of AEROSPACE ENGINEERING

*Proc IMechE Part G:
J Aerospace Engineering*
2016, Vol. 230(1) 157–171

DOI: 10.1177/0954410015588933
uk.sagepub.com/jaero
SAGE

Integrated flight/propulsion optimal control for DPC aircraft based on the GA-RPS algorithm

Jing Zhang, Wenwen Kang, Ang Li and Lingyu Yang

Abstract

The new distributed propulsion configuration (DPC) can effectively improve fuel efficiency and reduce pollution, but also brings in special cross-coupling effects between the flight and propulsion systems. To tackle this problem, integrated flight/propulsion modeling and optimal control of DPC with boundary layer ingestion (BLI) and supercirculation features are systematically investigated. As the basis, by taking the inherent BLI and supercirculation features into consideration, an integrated flight/propulsion model of SAX-40 is built to reflect the actual complex engine-aircraft coupling effects. Then an integrated flight/propulsion optimal control scheme is proposed to deal with the strong coupling effects and to implement the comprehensive control of redundant control surfaces as well as the distributed engines. Under this scheme, a detailed description of the optimal control problem is presented, and a novel two-stage optimization algorithm named genetic algorithm-random pattern search (GA-RPS) is proposed to solve this complex optimal problem. By the new strategies of "parallel genetic algorithm computing in sub-regions" and "random pattern search" in the GA-RPS algorithm, the optimization accuracy and convergence speed are effectively improved. Simulation results demonstrate the effectiveness of the GA-RPS algorithm and the significant performance improvement to DPC by optimization.

Keywords
Distributed propulsion configuration, integrated flight/propulsion control, optimization

Date received: 1 February 2015; accepted: 4 May 2015

Introduction

Conventional transport aircraft usually use the configuration of a tube-shaped fuselage and independently assembled wings, and this brings in a serious bottleneck when the aircraft's performance is to be improved. Moreover, environmental requirements for greener aviation lead to the innovative design of new aircraft. Distributed propulsion configuration (DPC) is a new integrated design provided for large airliners. This new configuration can effectively improve fuel efficiency, and reduce pollution and noise emission simultaneously. Undoubtedly, DPC has become the most promising development trend in commercial aviation.[1,2] DPC is composed of a blended wing body (BWB) layout and a distributed propulsion system (DPS). Its primary features include: (1) the semi-embedded inlets formed along the rear edge of the fuselage can ingest the boundary layer on the upper surface; (2) two-dimensional nozzles are installed to fulfill the thrust-vector technology.

Due to the integration of the BWB layout and the DPS in DPC, two new aerodynamic effects are introduced, namely boundary layer ingestion (BLI) and supercirculation. These two effects can improve the aerodynamic characteristics of DPC aircraft directly, but it also means that the propulsion system produces more complicated influences on the aerodynamic characteristics, resulting in an increased coupling effect between the engines and the aircraft. Due to this coupling effect, integrated flight/propulsion control technology is strongly demanded. Integrated flight/propulsion control (IFPC) can take the two new aerodynamic features into consideration, and implement integrated synchronous control of redundant control surfaces and the distributed engines. Considering the strong engine-aircraft coupling effect, IFPC is the only approach to achieve effective control of DPC aircraft and consequently improve the general aircraft performance.

School of Automation Science and Electrical Engineering, Beijing University of Aeronautics and Astronautics, China

Corresponding author:
Jing Zhang, School of Automation Science and Electrical Engineering, Beijing University of Aeronautics and Astronautics, The New Main Building E602, No.37, Xueyuan Road, Haidian District, Beijing 100191, China.
Email: zhangjing2013@buaa.edu.cn

For the novel DPC configuration, current scientific researches usually focus on the different integration designs and the corresponding BLI or supercirculation effects. NASA proposed a new "N+3" configuration in the final report by the Boeing subsonic ultra-green aircraft research team, in which significant improvements in aerodynamics, propulsion, and structures were pointed.[3] Kim and Liou[4] presented a flow simulation of an N3-X hybrid wing-body configuration, and the studies showed that the N3-X hybrid wing-body aircraft with turbo-electric distributed propulsion system could meet the environmental and performance goals of the N+3 generation transports. Another typical configuration is the "silent aircraft" proposed by Cambridge University and MIT. Related researches were pursued, including the design approaches, the multidisciplinary design and optimization procedures, the assessment of the available technologies, performance demonstration, etc.[5–10] Novel conceptual designs of an aircraft named SAX-40 with a calculated noise level of 62 dBA and high-fidelity simulations were discussed by Hileman.[11] Based on the above two configurations, extensive researches on DPC have been carried out to demonstrate the advanced designs, performance improvement, practicality, and potentiality of the distributed propulsion system.[12–28] As the important feature of DPC, BLI effect and the aerodynamic performance of a propulsion system were investigated by Plas.[29] A quantitative experiment on the "silent aircraft" showed that fuel consumption can be reduced by 3.8% due to the BLI effect. A conceptual design study to investigate the potential benefit of BLI with respect to the number of engines was conducted by Kok et al.,[30] who found that it may be better to focus on a small number of BLI engines since they do not suffer from high internal losses. Furthermore, researches were also carried out in other BLI research field, including the impact assessment of BLI on the engine's performance, inlet and nacelle design featuring BLI, and flow control in the inlet to decrease the adverse impact of BLI.[31–37] For the supercirculation effect, Capone[38] investigated the supercirculation effects induced by vectoring a partial-span rectangular jet. Besides, based on the NASA Langley national transonic facility semi-span FAST-MAC model, a circulation control flow scheme was developed by Jones and Miholen,[39] who also discussed the pneumatic flap performance for a two-dimensional circulation control airfoil.[40]

From the existing researches in this field, it can be observed that DPC designs and inherent BLI/ supercirculation features have become the main research area recently. However, as the most important characteristics of DPC aircraft, the complex coupling between the flight and propulsion systems is scarcely treated. Aiming at this problem, this article discusses the integrated flight/propulsion modeling and optimal control methods of DPC aircraft featuring BLI and supercirculation for the first time.

To conduct IFPC researches on DPC aircraft, a specific DPC aircraft SAX-40 is selected as the object. First, based on the BLI and supercirculation features calculated by computational fluid dynamics (CFD), an integrated flight/propulsion model is built to reflect the actual behavior of the whole system. Then, in consideration of the coupling characteristics and redundant control variables of the flight/propulsion system, an integrated flight/propulsion optimal control scheme is proposed, which can deal with the strong coupling effects effectively and implement comprehensive control of SAX-40. According to the scheme, a mathematical description of the optimization problem is presented to reduce the energy consumption during flight, then a new two-stage optimization method based on genetic algorithm and random pattern search (GA-RPS) is proposed to cope with the sharply increased number of optimization variables and constraints.

Modeling of integrated flight/propulsion system with BLI and supercirculation effects

SAX-40 is a prominent achievement of the Silent Aircraft Initiative program conducted by Cambridge University and MIT. The fuselage of SAX-40 is generated by stacked airfoils, and both the wings and center body can generate lift. As a consequence, the lift coefficient can be raised tremendously. SAX-40 has three sets of engines, and the control parameters of each set can be adjusted individually. Each set has three tunnels, with a turbofan in each tunnel providing the main thrust.[6,7]

The primary features of SAX-40 are: (1) The main control surfaces include the smoothly deflected leading-edge, three sets of hinged non-retractable flaps installed along each wing's rear-edge, and one set of rudders installed on the winglet. (2) Due to the semi-embedded inlets and the two-dimensional nozzles, BLI and supercirculation effects are certainly introduced. These two effects mainly influence the flight states and the control parameters of the distributed engines.

As analyzed above, the integrated flight/propulsion model (IFPM) of SAX-40 is built as in Figure 1. Flight states include airspeed, altitude and angle of attack. Propulsion's control variables include the pressure ratio of the turbofan, the nozzle exit area, and deflecting angles of the thrust. $\vec{F}$, $\vec{M}$ represent the total force and moment.

As shown in Figure 1, according to the BLI and supercirculation effects, control variables of the propulsion system can likely affect the aerodynamic characteristics, and generate direct control forces and moments through thrust vector simultaneously. Compared to the conventional configuration, the

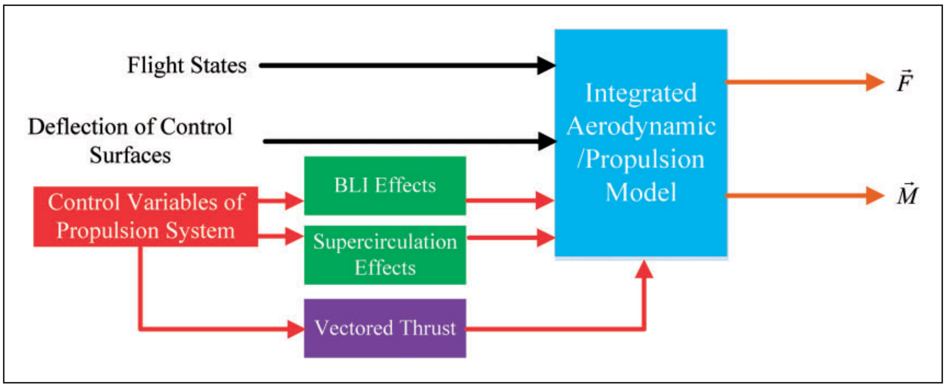

Figure 1. Integrated flight/propulsion model of SAX-40.

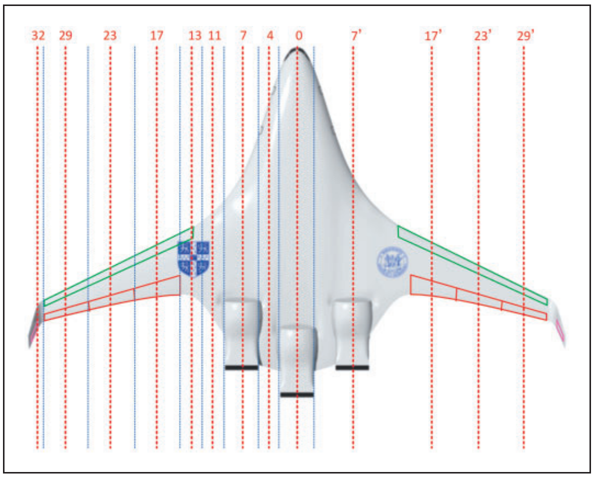

Figure 2. Sections arrangement on SAX-40.

interaction between flight and propulsion is more complicated on DPC aircraft.

The detailed modeling process of IFPM is shown as follows.

The aerodynamic model

According to the fundamental features of SAX-40, a stacked slices method is applied to build the quasi-3D model in this article. The advantages include: (1) BLI and supercirculation effects mainly act on the longitudinal axis, and the section models captured along the longitudinal axis can reflect these two effects authentically. (2) The section models consume less computational resources and, thus, more regularities of BLI and supercirculation effects can be obtained by different computations.

The arrangement of the sections on SAX-40 is shown in Figure 2. Each section represents an adjacent slice of the fuselage.

As BLI and supercirculation effects mainly act on the area before the inlets, the typical section 7 is selected as the primary section. The influence of BLI and supercirculation effects can be simulated by changing the section parameters $(T_{01}, P_{01}, q_{m01})$ and (T_8, P_8, V_8), which can be obtained by the DPS model. T, P, V, q_m represent static temperature, static pressure, velocity, and flow rate parameters in the engines respectively. Subscripts "01" and "8" represent engine's inlet and nozzle exit, respectively.

Based on the section arrangement of SAX-40, these sections can be separated into three categories, including clean airfoils, airfoils with the flap, and airfoils with the engine. Using the CFD method, the aerodynamic parameters of these airfoils can be obtained:

(a) The main influence factors on clean airfoils are the flight states, including the altitude H, the mach number Ma, the angle of attack α, and the pitching rate q.
(b) The main influence factors on airfoils with the flap also include the deflecting angle of the control surface δ_e.
(c) For the airfoils with the engine, apart from the basic flight states, the influence factors also include the control parameters of the engines, such as the pressure ratio of the turbofan π_k^*, the nozzle exit area A_8 , and the deflecting angle of the thrust α_T.

After the aerodynamic data of all sections are obtained, the quasi-3D aerodynamic model of SAX-40 is built as follows

$$\begin{aligned} C_l &= C_{l\_clean}(\alpha) + \sum_{i=1}^{3} C_{l\_DPS}^{\,i}\left(\alpha, \alpha_{Ti}, \pi_{ki}^*, A_{8i}\right) \\ &\quad + \sum_{j=1}^{6} C_{l\_Elev}^{\,j}\left(\alpha, \delta_{ej}\right) + C_{l\_q}(q) \\ C_d &= C_{d\_clean}(\alpha) + \sum_{i=1}^{3} C_{d\_DPS}^{\,i}\left(\alpha, \alpha_{Ti}, \pi_{ki}^*, A_{8i}\right) \\ &\quad + \sum_{j=1}^{6} C_{d\_Elev}^{\,j}\left(\alpha, \delta_{ej}\right) + C_{d\_q}(q) \\ C_m &= C_{m\_clean}(\alpha) + \sum_{i=1}^{3} C_{m\_DPS}^{\,i}\left(\alpha, \alpha_{Ti}, \pi_{ki}^*, A_{8i}\right) \\ &\quad + \sum_{j=1}^{6} C_{m\_Elev}^{\,j}\left(\alpha, \delta_{ej}\right) + C_{m\_q}(q) \end{aligned} \tag{1}$$

where C_l, C_d, C_m represent the lift, drag, and pitch moment coefficients, respectively. C_{l_clean} represents the lift coefficient from clean airfoils, including sections 4, 11, 13, and 32. $C_{l\_DPS}^{i}$ represents the lift coefficient from airfoils with the engine, including sections 0, 7, and 7′. BLI and supercirculation effects are reflected in this coefficient. $C_{l\_Elev}^{j}$ represents the lift coefficient from airfoils with the flap, including sections 17, 23, 29, 17′, 23′, and 29′. C_{l_q} represents the lift coefficient induced by q. Superscripts i and j represent the index of the engine and flap respectively. The compositions of C_d and C_m are similar.

Due to the introduction of BLI and supercirculation effects, $C_{l\_DPS}^{i}$ is more complicated, which can be described as

$$\begin{aligned} C_{l\_DPS}^{i}(\alpha,\alpha_{Ti},\pi_{ki}^{*},A_{8i}) &= C_{l\_0}(\alpha,\alpha_{Ti}) + \Delta C_{l\_BLI}(\pi_{ki}^{*},A_{8i}) \\ &\quad + \Delta C_{l\_V_8}(V_8) + \Delta C_{l\_\eta_{BLI}}(\eta_{BLI},\alpha_T) \end{aligned} \tag{2}$$

where C_{l_0} represents the basic lift coefficient. ΔC_{l_BLI} and $\Delta C_{l\_V_8}$ represent the lift increments generated by the BLI and jet inducing effects, and $\Delta C_{l\_\eta_{BLI}}$ represents the increment from the interaction between BLI and supercirculation. V_8 and η_{BLI} are the jet velocity and the BLI intensity respectively , which satisfy

$$\begin{aligned} V_8 &= V_8(\pi_k^{*},A_8) \\ \eta_{BLI} &= \eta_{BLI}(\pi_k^{*},A_8) \end{aligned} \tag{3}$$

The aerodynamic model shown in equations (1) and (2) can actually reflect the engine-aircraft coupling features of DPC aircraft, including the BLI and supercirculation effects.

The DPS model

As mentioned above, SAX-40 has three sets of engines. For one set, each tunnel of DPS consists of three primary parts, including the inlet, turbofan, and nozzle. In addition, there is a core engine providing the necessary power for all the three turbofans. The components in each set of DPS are shown in Figure 3.

As shown in Figure 3, "0" represents the entrance of the selected analysis region, which is located in the undisturbed airflow far ahead. "01" represents the entrance of the inlet. The area between "0" and "01" is named pre-compression segment. "1" and "2" represent the front and rear section of the fan, respectively. The inlet is located between "01" and "1". The turbofan is located between "1" and "2". "8" represents the exit of the nozzle, and the nozzle is located between "2" and "8".

The DPS model is built based on the inherent characteristics of all components, and the detailed modeling process of each tunnel is described as follows.

(a) Characteristic equations of components

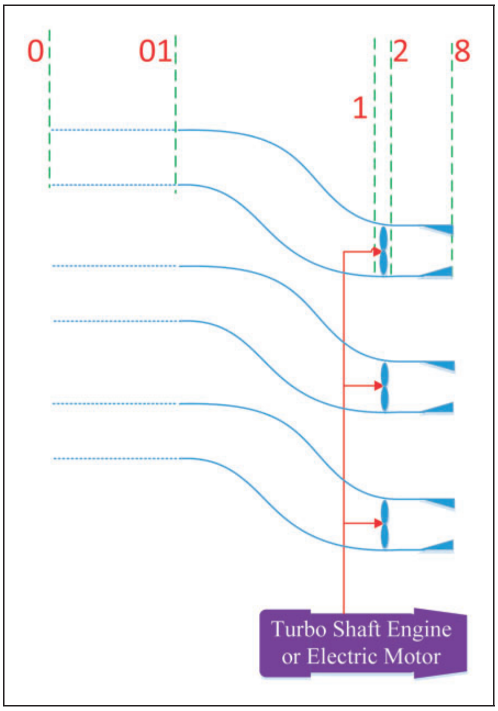

Figure 3. Illustrations of components in each set of engines.

The following assumptions on the thermodynamic process of each component are made: (1) The pre-compression segment is an adiabatic process, which means the total temperature and the total pressure in this segment are invariant. (2) There is a loss of total pressure in the inlet. (3) The fan is the main power-consuming component in each tunnel, and its pressure ratio is the main control parameter of the engine. (4) The nozzle is a convergent tube, and there is also a loss in the total pressure.

Based on the analysis of the thermodynamic process, characteristic equations of the components can be summarized as:

i. Pre-compression segment: $P_{01}^{*} = P_{0}^{*}, T_{01}^{*} = T_{0}^{*}$
ii. Inlet: $P_{1}^{*} = \sigma_i * P_{01}^{*},\ T_{1}^{*} = T_{01}^{*}$
iii. Fan: $P_{2}^{*} = \pi_k^{*} * P_{1}^{*},\ T_{2}^{*} = T_{1}^{*} * (\pi_k^{*})^{\frac{\gamma-1}{\gamma}}$
iv. Nozzle: $P_{8}^{*} = \sigma_e * P_{2}^{*}, T_{8}^{*} = T_{2}^{*}$

where P^{*}, T^{*} are the total pressure and the total temperature, respectively. The numbers in the subscripts represent the corresponding sections in Figure 3. σ_i, σ_e are the total pressure recovery coefficients of the inlet and the nozzle, respectively. γ is the specific heat ratio.

(b) Supplementary equations

The air mass flow rate at the inlet and outlet of each tunnel is invariant, and it can be described as

$$q_m = K\frac{P_{01}^{*} * A_{01} * q(\lambda_{01})}{\sqrt{T_{01}^{*}}} = K\frac{P_{8}^{*} * A_{8} * q(\lambda_{8})}{\sqrt{T_{8}^{*}}} \tag{4}$$

where K is the flow coefficient, and $K=\sqrt{\frac{\gamma}{R}\left(\frac{2}{\gamma+1}\right)^{\frac{\gamma+1}{\gamma-1}}}$. R is the gas constant. A_{01} refers to the cross section of the engine inlet. $q(\lambda)$ represents the flow function, which is defined as

$$q(\lambda)=\left(\frac{\gamma+1}{2}\right)^{\frac{1}{\gamma-1}}\lambda\left(1-\frac{\gamma-1}{\gamma+1}\lambda^{2}\right)^{\frac{1}{\gamma-1}} \tag{5}$$

where λ is the velocity coefficient.

Furthermore, the compressed air at A_8 should be checked whether it fully expands, and the corresponding expressions satisfy

$$\begin{cases} q(\lambda_8)=1 \quad \beta_8=\dfrac{P_0}{\sigma_e{}^*\sigma_i{}^*\pi_k^* * P_0^*}<\beta_{cr} \\ P_8=P_0 \quad \beta_8=\dfrac{P_0}{\sigma_e{}^*\sigma_i{}^*\pi_k^* * P_0^*}>\beta_{cr} \end{cases} \tag{6}$$

where P is the static pressure, β_{cr} is the critical pressure ratio of nozzle, and $\beta_{cr}=\left(\frac{2}{\gamma+1}\right)^{\frac{\gamma}{\gamma+1}}$.

(c) Thrust and power consumption

Based on the above characteristic and supplementary conditions, the thrust F and the power consumption P_{re} of each tunnel can be obtained

$$\begin{cases} F=q_{m0}{}^*(V_8-V_0)+A_8{}^*(P_8-P_0) \\ P_{re}=q_{m0}{}^*w_k \end{cases} \tag{7}$$

where V_0, q_{m0} represent the air velocity and mass flow rate at section "0". w_k means the power consumption with unit air mass flow rate, and it satisfies

$$w_k=\frac{\gamma}{\gamma-1}R*T_0^* * \left[\left(\pi_k^*\right)^{\frac{\gamma-1}{\gamma}}-1\right]/\eta_k^* \tag{8}$$

where η_k^* represents the efficiency of power transmission.

By synthesizing the feature equations for the components in all tunnels, a complete DPS model can be obtained. This model describes the relationships among the flight states (H,Ma), the control parameters (π_{ki}^*,A_{8i},$i=1,2,3$), and the output variables of the propulsion system, i.e. the section parameters, the total thrust, the total power consumption, and the BLI intensity.

In this paper, the BLI intensity η_{BLI} is defined as

$$\eta_{BLI}=\frac{A_0}{A_{01}}=\frac{q(\lambda_{01})}{q(\lambda_0)} \tag{9}$$

where A_0 refers to a cross section far ahead perpendicular to the air flow velocity with the same mass flow rate as A_{01}, as shown in Figure 4.

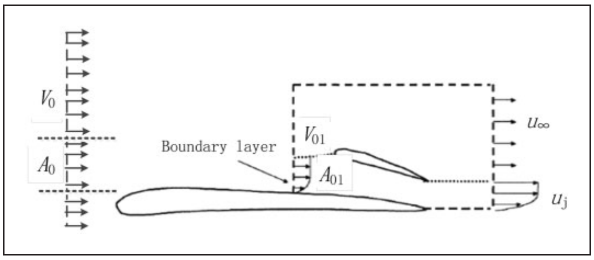

Figure 4. Illustrations of the BLI intensity.

Based on the above model, by combining all the three tunnels, the total direct forces and moment can be derived as

$$\begin{aligned} L_T&=T*\sin(\alpha+\alpha_T) \\ T_H&=T*\cos(\alpha+\alpha_T) \\ M_T&=T*\sin(\alpha_T)*L_1+T*\cos(\alpha_T)*L_2 \end{aligned} \tag{10}$$

where T represents the engine's thrust of each set, and L_T, T_H, M_T are the direct lift, the remained thrust, and the direct pitch moment respectively. An illustration of the relationships between T and L_T,T_H,M_T are shown in Figure 5.

Models integration

By synthesizing the aerodynamic force/moment ($\vec{F}_A$,$\vec{M}_A$) generated by the aerodynamic model and the direct force/moment ($\vec{F}_T$,$\vec{M}_T$) generated by the DPS model, the resultant force/moment of SAX-40 can be described as

$$\begin{aligned} \vec{F}&=\vec{F}_A+\vec{F}_T \\ \vec{M}&=\vec{M}_A+\vec{M}_T \end{aligned} \tag{11}$$

The projection of the IFPM's outputs in the velocity axis is shown in Figure 6.

Then, by taking the gravity Ginto consideration, the net lift L_R, thrust T_R , and moment M_R of SAX-40 can be described as follows

$$\begin{aligned} L_R&=L_A+L_T-G=L_R(\alpha,\pi_{k1}^*,A_{81},\alpha_{T1},\ldots,\delta_{e1},\ldots,) \\ T_R&=T_H-D_A=T_R(\alpha,\pi_{k1}^*,A_{81},\alpha_{T1},\ldots,\delta_{e1},\ldots,) \\ M_R&=M_A+M_T=M_R(\alpha,\pi_{k1}^*,A_{81},\alpha_{T1},\ldots,\delta_{e1},\ldots,) \end{aligned} \tag{12}$$

The scheme of IFPOC

For DPC aircraft, BLI and supercirculation effects can significantly change the aerodynamic characteristics, and the intensity of the two effects directly depends on the engine control parameters. This coupling effect makes the relationship between the flight and the propulsion systems more complex than conventional aircraft. Additionally, the increased number

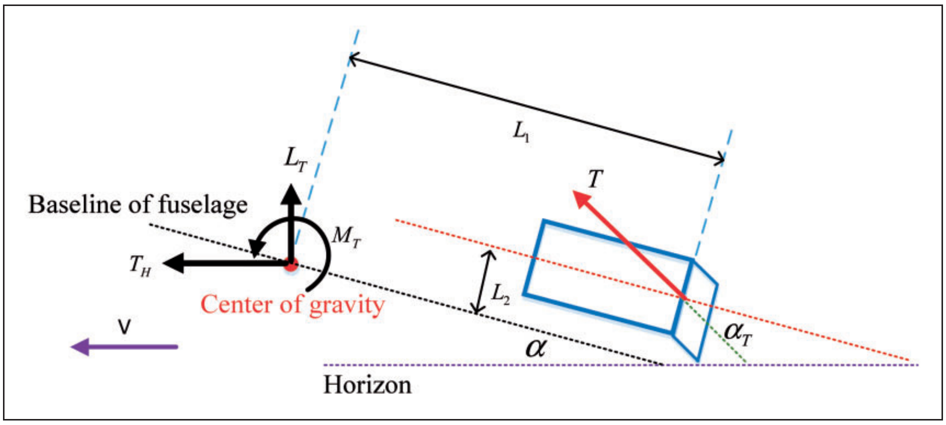

Figure 5. Direct forces and moment.

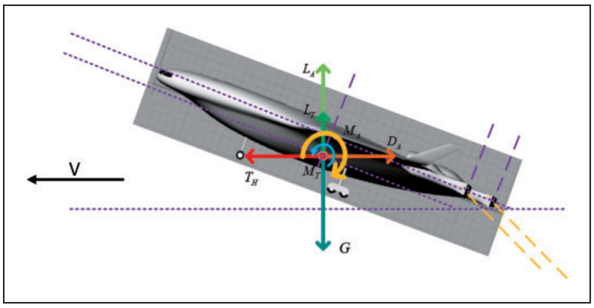

Figure 6. Projection of the IFPM's output. L_A, M_A, D_A represent the aerodynamic lift, moment, and drag, respectively.

of control parameters from the DPS and the flight control system may lead to further redundancy of control mechanisms. Facing these problems, the design strategy of integrated flight/propulsion optimal control, namely IFPOC, should be introduced for more effective control.

The overall structure of IFPOC is shown in Figure 7.

As shown in Figure 7, the whole scheme can be divided into four main parts: IFPM, the general and specific descriptions of the optimal control problem, and the optimization procedure.

IFPM includes the aerodynamics and the distributed propulsion models, and reflects the internal engine-aircraft coupling effects. For the distributed propulsion system, the main influences from the aerodynamic module are the different flight states, which can greatly change the propulsion's work condition. The primary flight states include the altitude, the Mach number, the pitch angle, etc. On the other hand, by ingesting the boundary layer flow on the upper fuselage surface into engine inlets, as well as two dimensional nozzles featuring the intense supercirculation around the middle of fuselage, distributed propulsion system can significantly improve the aerodynamic performance.

Based on IFPM, the general optimal control problem can be described for the particular optimization objective, such as the minimum energy consumption during flight. Consequently the specific optimal control problem can be derived according to the current flight condition. Finally, in accordance with the specific optimal control problem, control variables can be determined by the optimization procedure, and these commands will be sent to SAX-40's control surfaces and distributed engines to achieve optimal flight performance.

Design of IFPOC based on IFPM

A. Description of the general optimal control problem

In this paper, the required power P_R of SAX-40 is selected as the optimization objective. This parameter represents the amount of energy consuming during flight, and consequently it has a direct link to fuel consumption and also represents the economy index during flight.

Then the general optimal control problem is described as follows

$$\begin{aligned} &\min \quad P_R(\alpha, \pi^*_{k1}, A_{81}, \alpha_{T1}, \ldots, \delta_{e1}, \ldots,) \\ &s.t.\ L_R(\alpha, \pi^*_{k1}, A_{81}, \alpha_{T1}, \ldots, \delta_{e1}, \ldots,) = L_{Rc} \\ &\quad T_R(\alpha, \pi^*_{k1}, A_{81}, \alpha_{T1}, \ldots, \delta_{e1}, \ldots,) = T_{Rc} \\ &\quad M_R(\alpha, \pi^*_{k1}, A_{81}, \alpha_{T1}, \ldots, \delta_{e1}, \ldots,) = M_{Rc} \\ &\quad \alpha_l < \alpha < \alpha_u \\ &\quad \pi^*_{kl} < \pi^*_{ki} < \pi^*_{ku} \\ &\quad A_{8l} < A_{8i} < A_{8u} \\ &\quad \alpha_{Tl} < \alpha_{Ti} < \alpha_{Tu} \\ &\quad \delta_{el} < \delta_{ej} < \delta_{eu} \\ &\qquad i = 1, 2, 3, \quad j = 1, \ldots, 6 \end{aligned} \tag{13}$$

where L_{Rc}, T_{Rc}, M_{Rc} represent the net force and moment commands. α_l, α_u represent the lower and upper bounds of α respectively, and similar notations also apply to π^*_{ki}, A_{8i}, α_{Ti}, and δ_{ej}.

The optimization variables include the angle of attack α, control parameters of engines (π^*_{ki},A_{8i},α_{Ti}), and deflection angles of flaps δ_{ej}. Constraints include

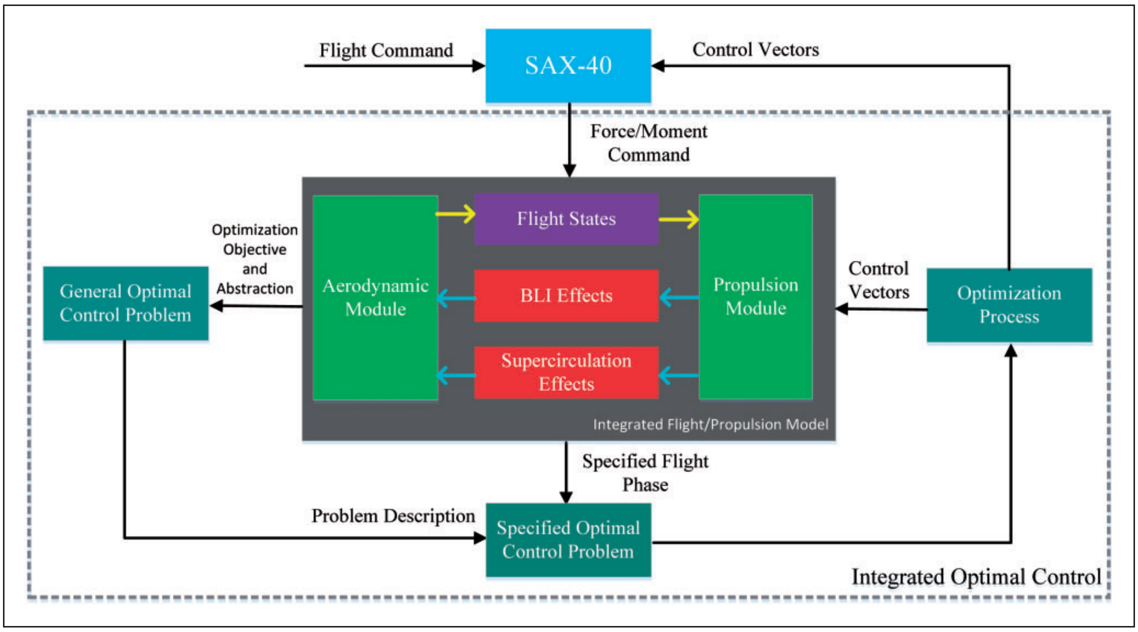

Figure 7. The scheme of IFPOC.

the equations of net force/moment and the feasible regions of all the optimization variables.

As described above, the general optimal control problem is a multi-constraints and multivariate optimization problem with strong nonlinearity. For this problem, traditional constrained optimization algorithms such as the penalty function method and the sequential quadratic programming method are not applicable. The reasons are: (1) These methods require the objective function $P_R\left(\alpha, \pi^*_{k1}, A_{81}, \alpha_{T1}, \ldots, \delta_{e1}, \ldots,\right)$ to have an explicit form. But due to the complexity of integrated flight/propulsion model, an explicit form may not be obtained with high accuracy. (2) The initial values may likely have a direct influence on the optimization results of these methods.

Genetic algorithm (GA) is an effective method for complicated optimization problems, and has drawn much attention recently. It provides a possibility to solve the complex optimization problem in this article. The advantages of GA include: (1) It operates directly on the objective function itself and explicit gradient is not required. (2) GA has a strong flexibility for different optimization problems. (3) Capability of parallel computing and the excellent ability of global optimization make GA the potential candidate for complicated nonconvex problems with large number of optimization variables. Because of these features, GA is an appropriate method to solve the optimization problem in equation (13). However, if the constraints are extremely strong, such as equality constraints, GA would soon encounter premature convergence, especially in highly nonlinear problems. Under the premature situation, GA will lose the ability of global optimization rapidly. Due to this disadvantage, the traditional GA method should be further improved for the optimization problem discussed.

B. A new GA-RPS algorithm

According to the primary advantages of GA, initial feasible solutions that satisfy the strict constraints can be found by GA rapidly. Then considering that the pattern search algorithm has strong searching ability for nonlinear problems, the optimal solution can be obtained exactly and quickly. The combination of GA and pattern search algorithm can effectively overcome the drawback of GA's premature convergence, and achieve improved accuracy and convergence speed.

Additionally, to overcome the premature convergence and maintain the gene diversity, some improvements are also introduced to GA: (1) Global mutation operation is applied to the DNA of best adaptive ones. (2) The way of chromosome chiasmata is heuristic to guarantee that the offspring has opportunities to get rid of the suppression from parental generation.

Therefore, a new two-stage optimization algorithm based on improved GA and random pattern search (RPS) is proposed, namely GA-RPS.

An illustration of GA-RPS is shown in Figure 8.

The first stage is parallel GA computing in subregions. According to the optimization objective P_R, the control vector is partitioned into n small subregions first. In each sub-region, a feasible solution $\boldsymbol{U}_k (k = 1, \ldots, n)$ is obtained by the improved GA algorithm and the corresponding required power P_{Rk} can be computed. By ranking all the solutions $\boldsymbol{U}_1, \ldots, \boldsymbol{U}_n$, the best feasible solution $\boldsymbol{U}_{opt}$ can be picked out. This feasible solution $\boldsymbol{U}_{opt}$ is located in

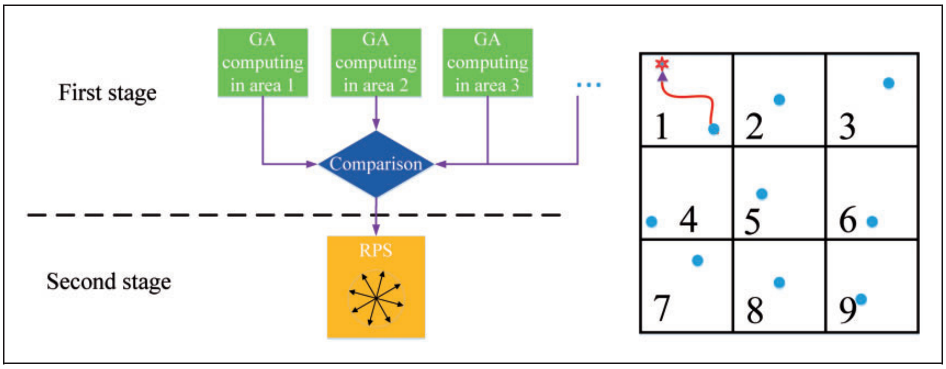

Figure 8. Illustration of the GA-RPS algorithm.

the neighborhood of the global optimal solution and considered as the initial value for the second stage. For example, as shown in Figure 8, the feasible solutions in different sub-regions are computed by the improved GA as Nos. 1–9, and $\boldsymbol{U}_1$ in sub-region 1 is selected as $\boldsymbol{U}_{opt}$ since it is closest to the global optimal solution.

By the strategy of parallel GA computing in sub-regions, an optimal feasible solution in the large optimization region can be found effectively, which guarantees the feasible solution to be placed near the global optimal point.

The second stage is random pattern search. To tackle the problem of explosive growth of search directions in fixed pattern search, a random pattern search strategy is proposed. This strategy can effectively reduce search directions and increase the probability of finding a feasible direction simultaneously. Uniformly distributed random numbers are utilized to generate unit search directions with uniform orientations. By the random strategy, the convergence speed can be improved obviously.

The detailed process of GA-RPS is described as the following steps:

The first stage: Parallel GA computing in sub-regions

(a) According to the current flight condition, the feasible regions of the control parameters are determined first, such as $\pi_{ki}^* \in \left(\pi_{kl}^*, \pi_{ku}^*\right)$, $A_{8i} \in (A_{8l}, A_{8u})$, $i = 1, 2, 3$. For one set of engines, the ranges of π_{ki}^* and A_{8i} can be divided into n_{1i} and n_{2i} parts respectively. As a consequence, the whole feasible region is partitioned into $N = \prod_{i=1}^{3} n_{1i}{}^* n_{2i}$ sub-regions.

(b) Parallel GA computing is conducted in each sub-region. For sub-region p ($p = 1, \ldots, N$), according to the sets of optimization variables, the real-coded method is utilized and DNA is assembled by all the variables directly, as

$$\boldsymbol{DNA} = \left[\alpha, \pi_{k1}^*, A_{81}, \alpha_{T1}, \ldots, \delta_{e1}, \ldots,\right] \tag{14}$$

(c) Merge the optimization objective and constraints into a fitness function

$$\max \, adaptValue = \frac{10^4}{\left\{ \begin{array}{l} P_R/sP_R + [(L_R - L_{Rc})/sL_R]^2 \\ +[(T_R - T_{Rc})/sT_R]^2 + [(M_R - M_{Rc})/sM_R]^2 \end{array} \right\}}$$

where sP_R represents the magnitude of P_R, and other variables are described similarly. The fitness function takes three aspects into consideration: (1) sP_R works as a scaling factor, such that the objective and constraints are converted into the same magnitude to ensure an equal level of impact. (2) All the net forces/moments are converted to be positive. (3) sL_R, sT_R, sM_R can be adjusted adaptively to enhance the influence of constraints.

(d) Uniform random numbers are used to initialize the population $G^0 = \{\boldsymbol{DNA}_1, \boldsymbol{DNA}_2, \ldots,\}$, and the initialization results are generated and distributed in the current optimization region.

(e) For generation k, evaluate and rank the DNAs in the current population $\boldsymbol{G}^k = \left\{\boldsymbol{DNA}_1^k, \boldsymbol{DNA}_2^k, \ldots,\right\}$ with the fitness function.

(f) According to the variation range Ran^k and the average value Ave^k of the quasi-optimal values in recent three generations $\boldsymbol{G}^{k-2}, \boldsymbol{G}^{k-1}, \boldsymbol{G}^k$ $(k \geqslant 2)$, judge if the GA computing has converged or not.

If $\delta^k = Ran^k / Ave^k < \varepsilon$, it means GA has converged. The optimal individual $\boldsymbol{DNA}_{opt}^k$ in $\boldsymbol{G}^k$ can be picked out, and consequently the feasible solution $\boldsymbol{DNA}_{fea}^p = \boldsymbol{DNA}_{opt}^k$ that satisfies the constraints is gained. Then GA computing in the current sub-region has ended.

If $\delta^k = Ran^k / Ave^k > \varepsilon$, it means GA computing has not converged, and the iteration continues.

(g) Conduct genetic operations on $\boldsymbol{G}^k$ to generate $\boldsymbol{G}^{k+1}$, including three operations:

   i. The optimal part of DNAs in $\boldsymbol{G}^k$ is reserved directly, and the global mutation is utilized as

$$\boldsymbol{DNA}' = \boldsymbol{DNA}_{ori} + \boldsymbol{\Delta}_{DNA} \tag{15}$$

where $\boldsymbol{DNA}'$ represents the updated individual after mutation, and $\boldsymbol{DNA}_{ori}$ represents the original one. Δ_{DNA} represents the random global mutation. The extent of Δ_{DNA} should be proper to maintain the optimality and gene diversity.

After this genetic operation, the DNAs obtained are described as $\boldsymbol{G}_{part1}^{k+1}$.

ii. To overcome the premature convergence issue, a heuristic arithmetic crossover operator is applied

$$\boldsymbol{Chi} = \lambda_p{}^{*}\boldsymbol{Par}_1 + (1-\lambda_p)^{*}\boldsymbol{Par}_2 \tag{16}$$

where $\lambda_p \in (-0.2, 1.2)$ is a random number. $\boldsymbol{Par}_1$ and $\boldsymbol{Par}_2$ represent the two parent DNAs, and $\boldsymbol{Chi}$ represents the new DNA generated by the two typical parent DNAs.

After this genetic operation, the DNAs obtained are described as $\boldsymbol{G}_{part2}^{k+1}$.

iii. Random mutation occurs on the single point of partial DNAs to ensure the diversity in the following generation. After this genetic operation, the DNAs obtained are described as $\boldsymbol{G}_{part3}^{k+1}$.

Then

$$\boldsymbol{G}^{k+1} = \boldsymbol{G}_{part1}^{k+1} + \boldsymbol{G}_{part2}^{k+1} + \boldsymbol{G}_{part3}^{k+1} \tag{17}$$

(h) After $\boldsymbol{G}^{k+1}$ is generated, go to step (e) and continue.

(i) After GA computing has completed in the N sub-regions, N feasible solutions can be acquired

$$\phi_{fea} = \left\{\boldsymbol{DNA}_{fea}^{1}, \ldots, \boldsymbol{DNA}_{fea}^{N}\right\} \tag{18}$$

And the required power corresponding to each feasible solution can be computed. $\boldsymbol{U}_{opt}$ with the lowest required power is pick out as the sub-optimal solution, which is also used as the initial value for the second stage optimization.

The second stage: Random pattern search

(a) Based on the initial value $\boldsymbol{U}^0 = \boldsymbol{U}_{opt}$, a basic step length λ^0 for search is selected empirically, which needs to guarantee the effectiveness of the first iteration and also avoid falling into the fake local optimal solution.

(b) For iteration k, determine the search pattern at the current feasible solution $\boldsymbol{U}^k$. M unit search directions are generated by uniform random numbers, described as

$$\Sigma^k = \left\{\boldsymbol{Dir}_1^k, \ldots, \boldsymbol{Dir}_M^k\right\} \tag{19}$$

Among them

$$\begin{aligned}\boldsymbol{Dir}_i^k &= \boldsymbol{D}_{temp\_i}^k / \left\|\boldsymbol{D}_{temp\_i}^k\right\|_2\\ \boldsymbol{D}_{temp\_i}^k &= \left[\Delta\alpha, \Delta\pi_{k1}^{*}, \Delta A8_1, \Delta\alpha_{T1}, \ldots, \Delta\delta_{e1}, \ldots,\right]\end{aligned} \tag{20}$$

These directions $\boldsymbol{Dir}_i^k$ have homogeneous orientations in the optimization region.

(c) Probe at $\boldsymbol{U}^k$ with the basic step length $\lambda^k = \lambda^0$ and the direction $\boldsymbol{Dir}_i^k$, then $\boldsymbol{U}_i^{k+1\prime}$ can be computed as:

$$\boldsymbol{U}_i^{k+1\prime} = \boldsymbol{U}^k + \lambda^k \boldsymbol{Dir}_i^k \tag{21}$$

Compute the required power $P_{Ri}^{k+1\prime}$ at $\boldsymbol{U}_i^{k+1\prime}$ and judge the contribution of directions Σ^k on minimizing the optimization objective. The reduction in the required power ΔP_{Ri}^k is described as

$$\Delta P_{Ri}^k = P_R^k - P_{Ri}^{k+1\prime}, \quad (i = 1, \ldots, M) \tag{22}$$

where P_R^k is the required power corresponding to $\boldsymbol{U}^k$.

Choose the direction which maximizes ΔP_{Ri}^k as the optimal search direction $\boldsymbol{Dir}_{opt}^k$, and continue.

If the optimal search direction in current search pattern does not exist, the step length will be further reduced as

$$\lambda_\nu^k = \nu^{*}\lambda^k \tag{23}$$

where ν is a scaling factor that satisfies $\nu < 1$. Take λ_ν^k as the step length and iterate this step until the optimal direction is found or λ_ν^k decreases enough to satisfy the convergence condition

$$\lambda_\nu^k < \vartheta \tag{24}$$

If the convergence condition is satisfied, the second optimization stage is completed and $\boldsymbol{U}^k$ is the global optimal solution $\boldsymbol{U}^*$.

(d) Based on the optimal search direction $\boldsymbol{Dir}_{opt}^k$ in step (c), increase the step length λ^k at $\boldsymbol{Dir}_{opt}^k$

$$\begin{aligned}\lambda_\mu^k &= \mu^{*}\lambda^k\\ \boldsymbol{U}_\mu^{k+1} &= \boldsymbol{U}^k + \boldsymbol{Dir}_{opt}^k * \lambda_\mu^k\end{aligned} \tag{25}$$

where μ is an enlarged scaling factor that satisfies $\mu > 1$. Iterate this step until the required power reaches the minimum value, then the feasible solution $\boldsymbol{U}^{k+1}$ can be obtained.

(e) Use $\boldsymbol{U}^{k+1}$ as the new initial value, and go to step (b) for another iteration.

The combination of parallel GA computing in sub-regions and random pattern search is appropriate as it gives full play to the primary advantages of these two algorithms: (1) RPS is highly effective for local search in a relative small region, and the strategy of parallel GA computing in sub-regions reasonably restricts the search area. (2) RPS needs a feasible initial solution, and the optimization in the first stage by the GA algorithm can just provide it.

Simulation and analysis

A. BLI and supercirculation effects

For BLI and supercirculation effects, the typical section 7 in Figure 2 is selected as the analysis area. Simulations are carried out under the condition $H = 10{,}000\,\mathrm{m}$, $Ma = 0.6$. Figure 9 shows the velocity and pressure nephograms of section "7" with clean airfoil and BLI effect.

As can be seen, the flow velocity on the upper surface of the airfoil is obviously raised with BLI effect, and consequently the static pressure on the upper surface decreases apparently. On the contrary, the static pressure of under surface increases distinctly. Compared to the clean airfoil, it can be deduced that the lift coefficient C_l increases and the aerodynamic characteristics is improved.

Under the same condition $H = 10{,}000\,\mathrm{m}$, $Ma = 0.6$, the jet velocity $V_8 = 285.3\,\mathrm{m/s}$ and the angle of attack $\alpha = 0^\circ$, the velocity nephograms under different thrust's deflection angles -7°, 0° are shown in Figure 10.

An obvious phenomenon is that when the thrust deflects downward, the inducing effect on the upper surface flow field is strong. When the thrust's deflection angle $\alpha_T = 0^\circ$, the lift coefficient C_l is 0.403. In comparison, the corresponding C_l is 0.651 as $\alpha_T = -7^\circ$. This means that the supercirculation effect induced by thrust vector can certainly improve C_l, and it has a great potential to make a lift augmentation system.

B. Comparisons of GA-RPS and GA methods

Simulations are carried out under a typical cruise condition $H = 10{,}000\,\mathrm{m}$, $Ma = 0.6$, and the net forces and moments of SAX-40 are all zero. Consequently, the right hand sides of the equality constraints in equation (13) are $L_{Rc} = 0$ N, $T_{Rc} = 0$ N, $M_{Rc} = 0$ Nm.

To reduce the number of optimization variables, some limitations are imposed to IFPM in the simulations, including:

(a) All the three sets of engines use the same control parameters π_k^*, A_8, α_T.

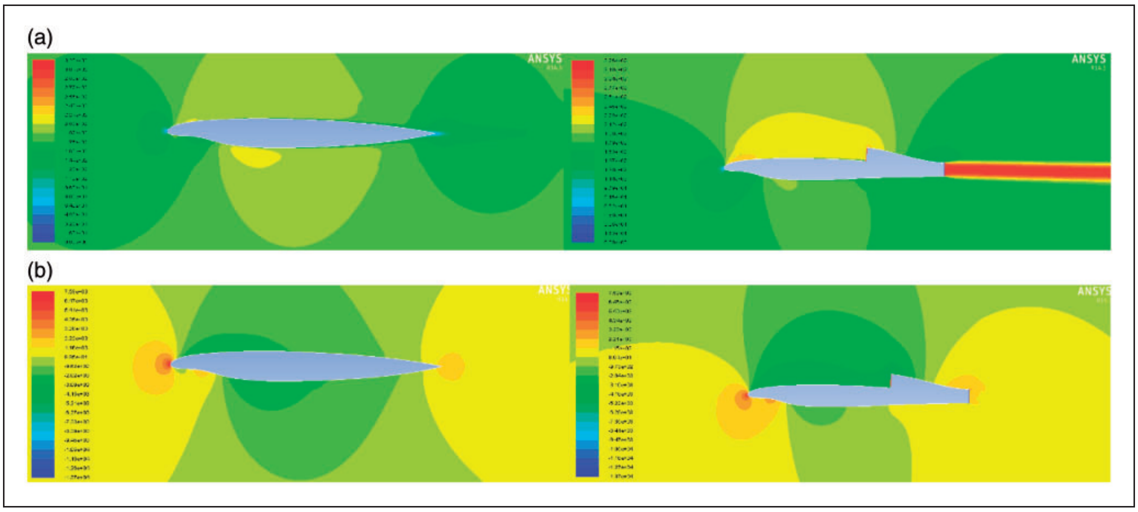

Figure 9. (a) Velocity and (b) pressure nephograms of BLI effect.

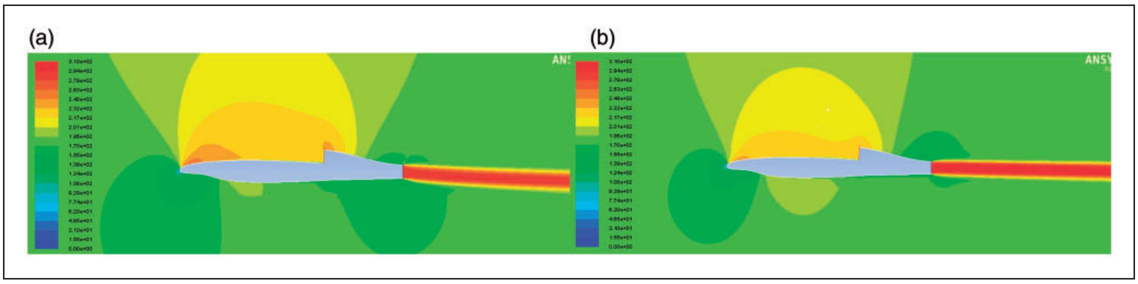

Figure 10. Velocity nephograms of supercirculation effect: (a) $\alpha_T = -7^\circ$; (b) $\alpha_T = 0^\circ$.

(b) All the three sets of flaps deflect synchronously, which means that all the flaps have the same deflecting angle $\delta_{e1} = \delta_{e1} = \cdots = \delta_{e6}$.

The optimal control problem is simplified under these limitations. Then, the specific optimal control problem for the cruise condition can be described as

$$\begin{aligned} \min \quad & P_R\left(\alpha, \pi_k^*, A_8, \alpha_T, \delta_e\right) \\ s.t. \ & L_R\left(\alpha, \pi_k^*, A_8, \alpha_T, \delta_e\right) = 0 \\ & T_R\left(\alpha, \pi_k^*, A_8, \alpha_T, \delta_e\right) = 0 \\ & M_R\left(\alpha, \pi_k^*, A_8, \alpha_T, \delta_e\right) = 0 \\ & -2^o < \alpha < 6^o \\ & 1.38 < \pi_k^* < 1.6 \\ & 1.4\text{m}^2 < A_8 < 1.6\text{m}^2 \\ & -7^o < \alpha_T < 5^o \\ & -25^o < \delta_e < 20^o \end{aligned} \tag{26}$$

The fitness function can be adjusted correspondingly

$$\max \quad adaptValue = \frac{10^4}{P_R/sP_R + (L_R/sL_R)^2 + (T_R/sT_R)^2 + (M_R/sM_R)^2}$$

Simulation results of the traditional GA algorithm for this problem are shown in Figure 11 depict the changes of the adapt value, the biases on the equality constraints $\Delta F, \Delta T, \Delta M$, and the objective function P_R with respect to the iteration number, respectively.

As can be seen, equality constraints can be satisfied quickly with the introduction of adaptive scale factors. However, both the adapt value and the objective P_R fluctuate with the variation of scale factors. The drastic changes indicate that the objective function has not sufficiently well represented in the fitness function and then could not converge. In summary, only the equality constraints are actually reflected in the fitness function, and the optimal solution could not

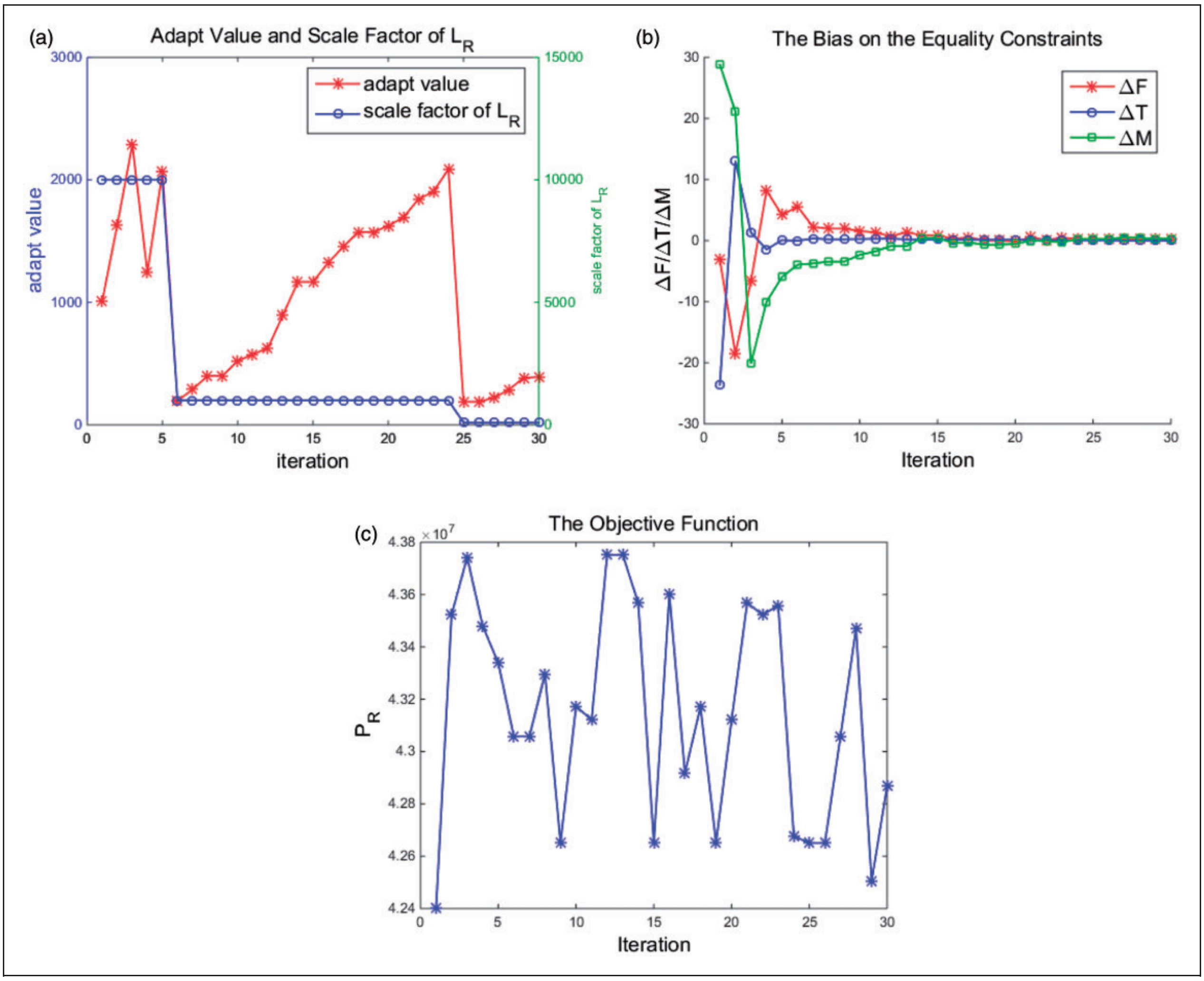

Figure 11. Simulation results of GA: (a) curve of the adapt value; (b) biases on the equality constraints; (c) the objective function.

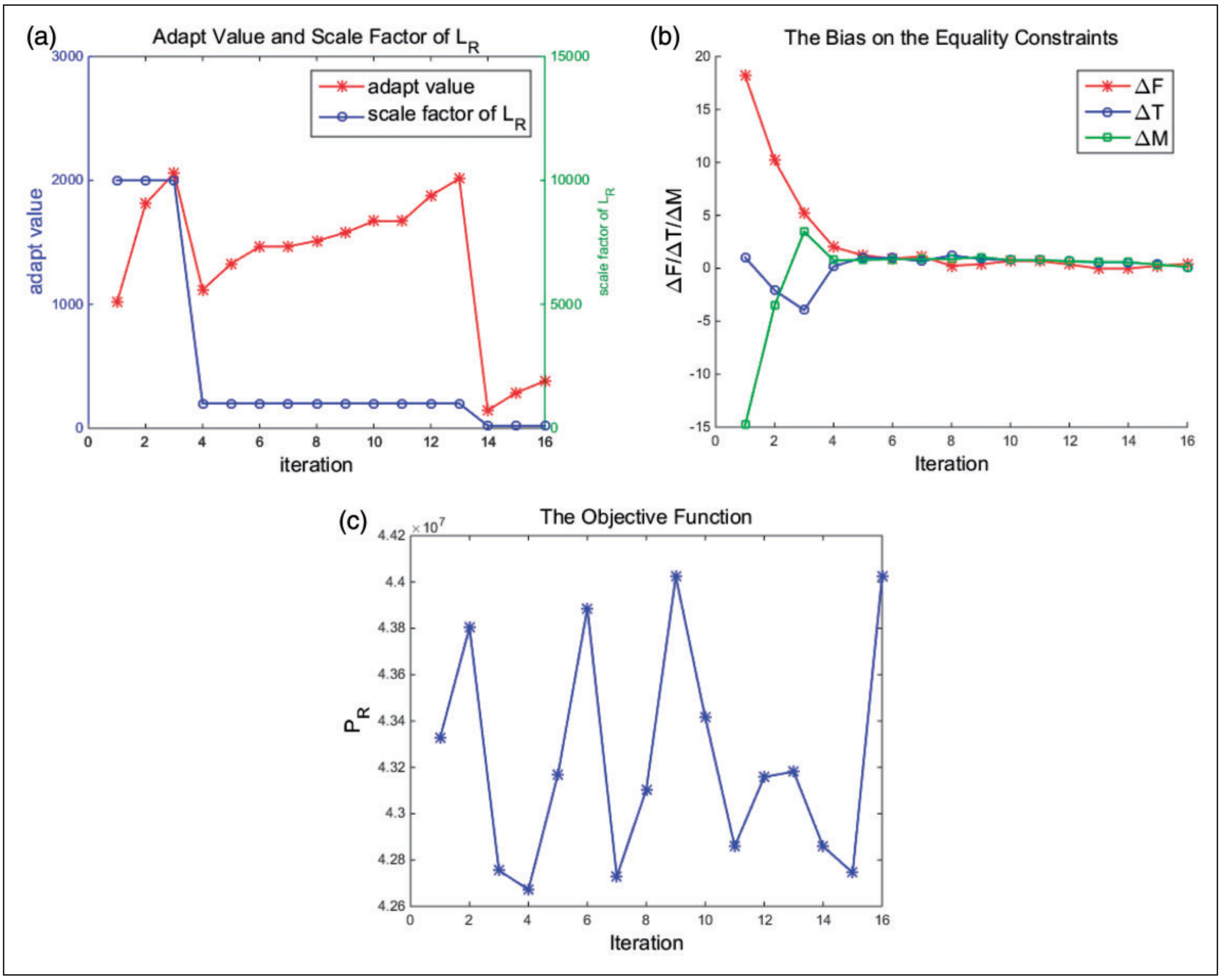

Figure 12. First optimization stage by parallel GA computing: (a) curve of the adapt value; (b) biases on the equality constraints; (c) the objective function.

be achieved. Apparently, the GA algorithm could hardly solve this optimal control problem properly.

Then the feasible regions of the control parameters π_k^*, A_8 are divided into nine sub-regions with a 3×3 grid while keeping the other variables fixed. The first optimization stage by parallel GA computing in the sub-regions (take one sub-region for example) is shown in Figure 12, and the second stage by random pattern search is shown in Figure 13.

As in Figures 12 and 13, compared with the 15 iterations by the GA algorithm, in the first stage of the GA-RPS algorithm, it only takes 5 iterations to obtain the feasible solution. It is obvious that the equality constraints are satisfied quickly, which means the strategy of the parallel GA computing in the sub-regions can find the feasible solutions effectively. In the second stage, the global optimal solution can be accurately obtained in about 50 iterations by RPS. Compared to the GA algorithm, the GA-RPS

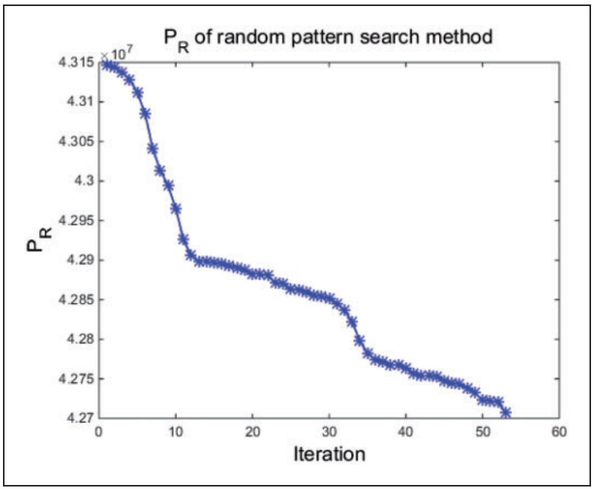

Figure 13. Second optimization stage by RPS.

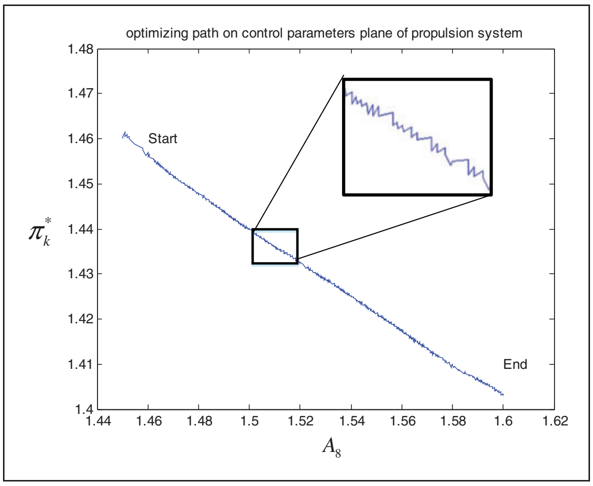

Figure 14. The optimizing path of linear search.

Table 1. Comparisons between GA-RPS and linear search.

Method	Time consumption	Restart or not?	Accuracy	Complexity
GA-RPS	3 min	No	5% of Error	High
Linear search	4 h	Yes	5% of Error	Low

algorithm can solve the optimal control problem more effectively, and improve the accuracy and convergence speed simultaneously.

C. Comparisons of GA-RPS and linear search method

For the optimal control problem described in equation (26), the optimizing path of the linear search method is shown as Figure 14.

As can be seen, the optimizing path of the linear search method is very tortuous, and the computing time is unacceptable. Detailed comparisons between the GA-RPS and the linear search are shown in Table 1.

As can be seen, compared to the linear search method, GA-RPS is more efficient and applicable to the complex integrated flight/propulsion optimal control problem.

D. Analysis of performance improvements

For the traditional GA algorithm, the feasible solution obtained is

$$\begin{aligned} \boldsymbol{U} &= \left[\alpha, \pi_k^*, A_8, \alpha_T, \delta_e\right] \\ &= \left[2.8479^\circ \quad 1.4388 \quad 1.5048\,\mathrm{m}^2 \quad 0.1130^\circ \quad 0.9199^\circ\right] \end{aligned}$$

The corresponding required power is $P_R = 4.4596 \times 10^7$ W and the BLI intensity is $\eta_{BLI} = 1.088$.

In contrast, the optimal feasible solution in the first stage of GA-RPS is

$$\begin{aligned} \boldsymbol{U} &= \left[\alpha, \pi_k^*, A_8, \alpha_T, \delta_e\right] \\ &= \left[2.6664^\circ \quad 1.4067 \quad 1.5850\,\mathrm{m}^2 \quad 1.4624^\circ \quad 0.9275^\circ\right] \end{aligned}$$

the corresponding required power is $P_R = 4.2954 \times 10^7$ W and the BLI intensity is $\eta_{BLI} = 1.120$.

The global optimal solution in the second stage is

$$\begin{aligned} \boldsymbol{U} &= \left[\alpha, \pi_k^*, A_8, \alpha_T, \delta_e\right] \\ &= \left[2.5272^\circ \quad 1.4022 \quad 1.5952\,\mathrm{m}^2 \quad 2.8459^\circ \quad 0.9324^\circ\right] \end{aligned}$$

The corresponding required power is $P_R = 4.2741 \times 10^7$Wand the BLI intensity is $\eta_{BLI} = 1.124$.

As above, the required power P_R obtained by the traditional GA algorithm is 4.4596×10^7, and the corresponding data for the global optimal solution of GA-RPS is 4.2741×10^7. Compared to the GA algorithm, P_R obtained by GA-RPS is 4.16% lower, which indicates less fuel consumption during flight and demonstrates the superiority of GA-RPS. Additionally, in the different stages of GA-RPS, P_R is 4.2954×10^7,4.2741×10^7 respectively, and the required power can be further reduced by 0.5%. These results demonstrate that SAX-40 has tremendous energy-saving potential and an appropriate optimization algorithm is extremely essential.

Moreover, the BLI intensity η_{BLI} obtained by GA is 1.088. In the first stage of GA-RPS, the best feasible solution has the corresponding BLI intensity $\eta_{BLI} = 1.120$ and in the second stage the global optimal solution has the highest BLI intensity $\eta_{BLI} = 1.124$. In comparison, it can be deduced that the optimization procedure is marching towards the direction of intensifying BLI effect. Similarly, comparing the thrust's deflection angles α_T of different methods, we can find that the optimal solution has the largest deflection angle $\alpha_T = 2.8459^\circ$. This indicates the strongest supercirculation effect. Therefore, the optimization process is also driven by intensifying supercirculation effect.

In conclusion, BLI and supercirculation effects play a very important role in the performance improvement of SAX-40. By utilizing the BLI and supercirculation effects sufficiently, energy consumption in flight can be reduced significantly, which makes DPC aircraft more competitive.

Conclusion

This article focuses on the integrated flight/propulsion control technology of distributed propulsion configuration aircraft. Based on the inherent BLI and supercirculation features, an integrated flight/propulsion model is developed. After that, to deal with the strong cross-coupling between aircraft and engines, an integrated flight/propulsion optimal control scheme is presented, and a new two-stage optimization algorithm named genetic algorithm-random pattern search is proposed to solve this complex optimization problem with improved accuracy and convergence speed. Simulation results demonstrate the effectiveness of this approach.

From the detailed analysis, several significant conclusions can be derived: (1) BLI and supercirculation effects are exactly beneficial features for DPC. By using the two effects properly, fuel efficiency can be obviously improved. (2) DPC aircraft have a great capacity of performance improvement through optimization. However, due to the complexity of DPC aircraft, it requires an effective integrated flight/propulsion optimal control method to fully exploit the potential.

Conflict of interest

None declared.

Funding

This work was supported by the National Natural Science Foundation of China (Grant No.61304030) and the Aviation Science Foundation (Grant No.20135851041).

References

1. Dangelo MM. N+3 small commercial efficient and quiet transportation for year 2030–2035. Report, NASA/CR-2010-216691, US, May 2010.
2. Liebeck RH. Design of the blended wing body subsonic transport. *J Aircraft* 2004; 41: 10–25.
3. Bradley MK and Droney CK. Subsonic ultra green aircraft research: Phase I final report. Report, NASA/CR-2011-216847, US, April 2011.
4. Kim H and Liou MS. Flow simulation of N3–X hybrid wing-body configuration. In: *The 51st AIAA aerospace sciences meeting including the new horizons forum and aerospace exposition*, Grapevine, TX, USA, 7–10 January 2013, paper no. AIAA Paper 2013-221, pp.1–18.
5. Hileman JI, Reynolds TG, Blanco ER, et al. Development of approach procedures for silent aircraft. In: *The 45th AIAA aerospace sciences meeting and exhibit*, Reno, NV, USA, 8–11 January 2007, paper no. AIAA Paper 2007-451, pp.1–14.
6. Diedrich A, Hileman J, Tan D, et al. Multidisciplinary design and optimization of the silent aircraft. In: *The 44th AIAA aerospace sciences meeting and exhibit*, Reno, NV, USA, 9–12 January 2006, paper no. AIAA Paper 2006-1323, pp.1–12.
7. Dowling A and Greitzer E. The silent aircraft initiative–overview. Report for the 45th AIAA Aerospace Sciences Meeting, Reno, NV, USA, January 2007.
8. Hall CA, Schwartz E and Hileman JI. Assessment of technologies for the silent aircraft initiative. *J Propul Power* 2009; 25: 1153–1162.
9. Hileman JI, Spakovszky ZS, Drela M, et al. Aerodynamic and aeroacoustic three-dimensional design for a "silent" aircraft. In: *The 44th AIAA aerospace sciences meeting and exhibit*, Reno, NV, USA, 9–12 January 2006, paper no. AIAA Paper 2006-241, pp.1–15.
10. Liu Y, Dowling AP, Hileman JI, et al. Surface roughness noise prediction for silent aircraft experimental design SAX-40. In: *The 46th AIAA aerospace sciences meeting and exhibit*, Reno, NV, USA, 7–10 January 2008, paper no. AIAA Paper 2008-45, pp.1–13.
11. Hileman JI, Spakovszky ZS and Drela M. Airframe design for silent aircraft. In: *The 45th AIAA aerospace sciences meeting and exhibit*, Reno, NV, USA, 8–11 January 2007, paper no. AIAA Paper 2007-453, pp.1–15.
12. Gohardani A, Doulgeris G and Singh R. Challenges of future aircraft propulsion: A review of distributed propulsion technology and its potential application for the all-electric commercial aircraft. *Prog Aerosp Sci* 2011; 47: 369–391.
13. Kim HD. Distributed propulsion vehicles. In: *The 27th international congress of the aeronautical sciences*, Nice, France, 19–24 September 2010, pp.1–11.
14. Schiltgen B, Green MW, Gibson AR, et al. Benefits and concerns of hybrid electric distributed propulsion with conventional electric machines. In: *The 48th AIAA/ASME/SAE/ ASEE joint propulsion conference & exhibit*, Atlanta, GA, USA, 30 July to 1 August 2012, paper no. AIAA Paper 2012-3769, pp.1–19.
15. Gibson AR, Hall D, Waters M, et al. The potential and challenge of turbo electric propulsion for subsonic transport aircraft. In: *The 48th AIAA aerospace sciences meeting including the new horizons forum and aerospace exposition*, Orlando, FL, USA, 4–7 January 2010, paper no. AIAA Paper 2010-276, pp.1–22.
16. Kim HD, Brown GV and Felder JL. Distributed turboelectric propulsion for hybrid wing body aircraft. In: *The 2008 International powered lift conference*, London, UK, 22–24 July 2008, pp.1–11.
17. Felder JL, Tong MT and Chu JL. Sensitivity of mission energy consumption to turboelectric distributed propulsion design assumptions on the N3-X hybrid wing body aircraft. In: *The 48th AIAA/ASME/SAE/ASEE joint propulsion conference & exhibit*, Atlanta, GA, USA, 30 July to 1 August 2012, paper no. AIAA Paper 2012-3701, pp.1–14.
18. Sands JS, Gladiny JC and Kestnerz BK. Hybrid wing body engine cycle design exploration for boundary layer ingesting (BLI) propulsion systems under design uncertainty. In: *The 48th AIAA/ASME/SAE/ASEE joint propulsion conference & exhibit*, Atlanta, GA, USA, 30 July to 1 August 2012, paper no. AIAA Paper 2012-3918, pp.1–17.
19. Ameyugo G, Taylor M and Singh R. Distributed propulsion feasibility studies. In: *The 25th International congress of the aeronautical sciences*, Hamburg, Germany, 3–8 September 2006, pp.1–10.
20. Kim HD and Saunders JD. Embedded wing propulsion conceptual study. Report, NASA/TM-2003-212696, US, November 2003.
21. Felder JL, Kim HD, Brown GV, et al. An examination of the effect of boundary layer ingestion on turboelectric distributed propulsion systems. In: *The 49th AIAA aerospace sciences meeting including the new horizons forum and aerospace exposition*, Orlando, FL, USA,

4–7 January 2011, paper no. AIAA Paper 2011-300, pp.1–26.

22. Liu CY, Doulgeris G, Laskaridis P, et al. Thermal cycle analysis of turboelectric distributed propulsion system with boundary layer ingestion. *Aerosp Sci Technol* 2013; 27: 163–170.
23. Liu CY, Doulgeris G, Laskaridis P, et al. Turboelectric distributed propulsion system modelling for hybrid-wing-body aircraft. In: *The 48thAIAA/ASME/SAE/ASEE joint propulsion conference & exhibit*, Atlanta, GA, USA, 30 July to 1 August 2012, paper no. AIAA Paper 2012-3700, pp.1–13.
24. Blanco ER, Hall CA and Crichton D. Challenges in the silent aircraft engine design. In: *The 45th AIAA aerospace sciences meeting and exhibit*, Reno, NV, USA, 8–11 January 2007, paper no. AIAA Paper 2007-454, pp.1–20.
25. Andy K, Schetz JA and Mason WH. Assessment of the potential advantages of distributed-propulsion for aircraft. Report, ISABE-2003-1094, 2003.
26. Andy K, Leifsson LT, Mason WH, et al. MDO of a blended-wing-body transport aircraft with distributed propulsion. In: *The AIAA's 3rd annual aviation technology, integration, and operations*, Denver, CO, USA, 17–19 November 2003, paper no. AIAA Paper 2003-6732, pp.1–11.
27. Yaros SF, Sexstone MG, Huebner LD, et al. Synergistic airframe-propulsion interactions and integrations. Report, NASA/TM-1998-207644, March 1998.
28. Schetz JA, Hosder S and Dippold V. Propulsion and aerodynamic performance evaluation of jet-wing distributed propulsion. *Aerosp Sci Technol* 2010; 14: 1–10.
29. Plas A. *Performance of a boundary layer ingesting propulsion system*. Master Thesis, Massachusetts Institute of Technology, MA, USA, 2006.
30. Kok HJ, Voskuijl M and Tooren MJ. Distributed propulsion featuring boundary layer ingestion engines for the blended wing body subsonic transport. In: *The 51st AIAA/ASME/ASCE/AHS/ ASC structures, structural dynamics and materials conference*, Orlando, FL, USA, 12–15 April 2010, paper no. AIAA Paper 2010-3064, pp.1–12.
31. Lugo VM, Doulgeris G and Singh R. Computational analysis of the effects of a boundary layer ingesting propulsion system in transonic flow. *Proc IMechE, Part G: J Aerospace Engineering* 2012; 227: 1215–1232.
32. Smith LH. Wake ingestion propulsion benefit. *J Propul Power* 1993; 9: 74–82.
33. Rodriguez DL. A multidisciplinary optimization method for designing boundary layer ingesting inlets. Report, AIAA-2002-5665, 2002.
34. Johnson BC, Webster RS and Sreenivas K. A numerical investigation of S-duct flows with boundary-layer ingestion. In: *The 48th AIAA aerospace sciences meeting including the new horizons forum and aerospace exposition*, Orlando, FL, USA, 4–7 January 2010, paper no. AIAA Paper 2010-841, pp.1–12.
35. Lee BJ and Liou MS. Optimizing a boundary-layer-ingestion offset inlet by discrete adjoint approach. *AIAA J* 2010; 48: 2008–2016.
36. Owens LR, Allan BG and Gorton SA. Boundary-layer-ingesting inlet flow control. *J Aircraft* 2008; 45: 1431–1440.
37. Allan BG and Owens LR. Numerical modeling of flow control in a boundary-layer-ingesting offset inlet diffuser at transonic Mach numbers. In: *The 44th AIAA aerospace sciences meeting and exhibit*, Reno, NV, USA, 9–12 January 2006, paper no. AIAA Paper 2006-845, pp.1–25.
38. Capone FJ. Supercirculation effects induced by vectoring a partial-span rectangular jet. *J Aircraft* 1975; 12: 633–638.
39. Jones GS and Miholen WE. Development of the circulation control flow scheme used in the NTF Semi-span FAST-MAC model. In: *The 31st AIAA applied aerodynamics conference*, San Diego, CA, USA, 24–27 June 2013, paper no. AIAA Paper 2013-3048, pp.1–20.
40. Jones GS. Pneumatic flap performance for a 2D circulation control airfoil, steady & pulsed. Report, NASA/ONR circulation control workshop, NASACP-2005-213509, US, 2004.